Microstructures

Research Article

Layer modulating and electrical properties in acceptor-doped $Sr_5Nb_5O_{17}$ ceramic with perovskite layer structure

Xiaoxu Duan[1], Jungu Xu[1], Xianfeng Yang[2], Xiaoling He[3], Cheng Wang[1], Laijun Liu[1]

[1]MOE Key Laboratory of New Processing Technology for Nonferrous Metals and Materials, Guangxi Universities Key Laboratory of Non-ferrous Metal Oxide Electronic Functional Materials and Devices, College of Materials Science and Engineering, Collaborative Innovation Center for Exploration of Nonferrous Metal Deposits and Efficient Utilization of Resources, Guilin University of Technology, Guilin 541004, Guangxi, China.
[2]Analytical and Testing Centre, South China University of Technology, Guangzhou 510640, Guangdong, China.
[3]Guangxi Key Laboratory of Superhard Materials, China Nonferrous Metals (Guilin) Geology and Mining Co., Ltd, Guilin 541004, Guangxi, China.

Correspondence to: Prof./Dr. Jungu Xu, MOE Key Laboratory of New Processing Technology for Nonferrous Metals and Materials, Guangxi Universities Key Laboratory of Non-ferrous Metal Oxide Electronic Functional Materials and Devices, College of Materials Science and Engineering, Collaborative Innovation Center for Exploration of Nonferrous Metal Deposits and Efficient Utilization of Resources, No. 12, Jiangan Road, Guilin University of Technology, Guilin 541004, Guangxi, China. E-mail: xujungu@glut.edu.cn; Prof./Dr. Xianfeng Yang, Analytical and Testing Centre, South China University of Technology, Guangzhou 510640, Guangdong, China. E-mail: czxfyang@scut.edu.cn; Prof./Dr. Laijun Liu, MOE Key Laboratory of New Processing Technology for Nonferrous Metals and Materials, Guangxi Universities Key Laboratory of Non-ferrous Metal Oxide Electronic Functional Materials and Devices, College of Materials Science and Engineering, Collaborative Innovation Center for Exploration of Nonferrous Metal Deposits and Efficient Utilization of Resources, No. 12, Jiangan Road, Guilin University of Technology, Guilin 541004, Guangxi, China. E-mail: ljliu2@163.com

Abstract

Perovskite layer structured (PLS) oxides exhibit some novel physical properties, such as ultrahigh-temperature piezoelectricity, semiconductivity, and oxygen ionic transport. However, synthesizing 5-layer PLS oxides, such as $Sr_5Nb_5O_{17}$ ceramics, using traditional solid-state reaction methods is challenging due to their low phase stability. In this study, we propose a new strategy to construct a 5-layer structure from a 4-layer structure. Specifically, Ga-doped $Sr_5Nb_{4.444}Ga_{0.556}O_{16.944}$ (5-SNGO), an iso-structural material to $Sr_5Nb_5O_{17}$, was synthesized via a solid-phase reaction. The original design involved co-doping Ga and Mo at the Nb site of the 4-layer parent material $Sr_2Nb_2O_7$

(4-SNO). However, it was found that only Ga was successfully incorporated into the structure, while Mo remained as $SrMoO_4$, which was subsequently removed by washing with dilute sulfuric acid. X-ray diffraction, transmission electron microscopy, and second-harmonic generation analysis confirmed that the synthesized 5-SNGO ceramic exhibits a 5-layer structure with a noncentrosymmetric space group. The material demonstrated a frequency-independent dielectric permittivity of 60 above 1 kHz. Impedance spectroscopy revealed a very high resistivity of 1.95×10^5 $\Omega \cdot$cm at 900 °C, along with Debye-like dielectric relaxation exhibiting thermal activation behavior. This study presents a novel synthesis approach for constructing 5-layer PLS oxides from a 4-layer structure and provides insights into their structural evolution and electrical properties.

Keywords: Perovskite layer structured, solid-phase reaction, $Sr_2Nb_2O_7$, $Sr_5Nb_5O_{17}$, ferroelectric properties

INTRODUCTION

As a new type of functional material, layered niobate compounds have attracted much attention for exhibiting special chemical properties in the fields of photocatalysis, ion exchange, high-temperature piezoelectricity, electrochemistry, and photoluminescence[1-6]. The layered niobate compounds belong to the group of perovskite layer structured compounds with the general formula $A_nB_nO_{3n+2}$ (A = Sr, Ca, La; B = Nb, Ta, Ti), which is a layered structure consisting of chalcogenide units stacked by corner-shared BO_6 octahedra and 12-coordinated A cations, with n denoting the number of oxygen octahedra per layer, i.e., the number of layers. The chemical formula $Sr_nNb_nO_{3n+2}$ is often denoted as strontium niobate compound $(SrNbO_x)$[7]. The crystal structure and physical properties of these compounds are determined by their oxygen content; thus, a small change in the oxygen content can be used to regulate their atomic structure and physical properties. The two most representative compounds in the $Sr_nNb_nO_{3n+2}$ family are $Sr_2Nb_2O_7$ $(=Sr_4Nb_4O_{14}$, $n = 4$, $SrNbO_{3.5}$, Figure 1A) and $Sr_5Nb_5O_{17}$ $(n = 5$, $SrNbO_{3.4}$, Figure 1B)[7,8]. $Sr_5Nb_5O_{17}$ exhibits highly anisotropic quasi-one-dimensional conductivity, with the highest conductivity along the a-axis, displaying distinct metallic conduction characteristics[9]. This conductivity originates from the relatively lower-valent Nb ions (averaged in +4.8), which possess partially occupied 4d orbital electrons, as well as from the distortion-free NbO_6 ortho-octahedra in the conductive layer, where Nb ions are centrally located within the octahedra[10]. In contrast, $Sr_2Nb_2O_7$ contains Nb cations exclusively in the +5 oxidation state. The Nb ions within its NbO_6 octahedra are far from the octahedral center, resulting in pronounced distortions[6,11]. Additionally, Sr atoms in this compound occupy two distinct crystallographic positions: Sr1 at the boundary of the chalcocite layer, and Sr2 inside the chalcocite layer[6]. In $Sr_5Nb_5O_{17}$, however, there are three crystallographic sites for Sr atoms: Sr1 is positioned at the boundary of the chalcocite layer, similar to $Sr_4Nb_4O_{14}$, while Sr2 and Sr3 are both located inside the chalcocite layer. The key distinction is that Sr2 and Sr3 are coordinated by 10 and 9 O atoms, respectively, with Sr-O distances ranging from 2.64(1) to 2.89(1) for Sr2 and from 2.50(1) to 2.90(1) for Sr3.

As a multifunctional compound, $Sr_2Nb_2O_7$ has been extensively studied for its oxygen ion conductivity, dielectric, piezoelectric, and photocatalytic properties, among others[6,12-20]. Notably, $Sr_2Nb_2O_7$ exhibits high chemical and thermal stability, along with excellent piezoelectric properties and a high Curie temperature $(T_c > 1,300$ °C). With the in-depth study of oxygen ionic conductors, it has been realized that the introduction of oxygen vacancies through low-valent cation doping is one of the most direct and effective ways for modifying the electrical properties of these materials[21-23]. Previous works have shown that the electrical properties of $Sr_nNb_nO_{3n+2}$ compounds can be modulated in several ways[24-27]. One approach involves elemental doping or irradiation-induced phase transformation[24,26], while another focuses on modifying the morphology of NbO_6 octahedra to achieve the desired electrical properties[25]. However, previous studies have revealed that low-valent single doping at the Sr and Nb sites makes it hard to synthesize a single-phase material and fails to significantly improve its electrical properties[28]. Therefore, co-
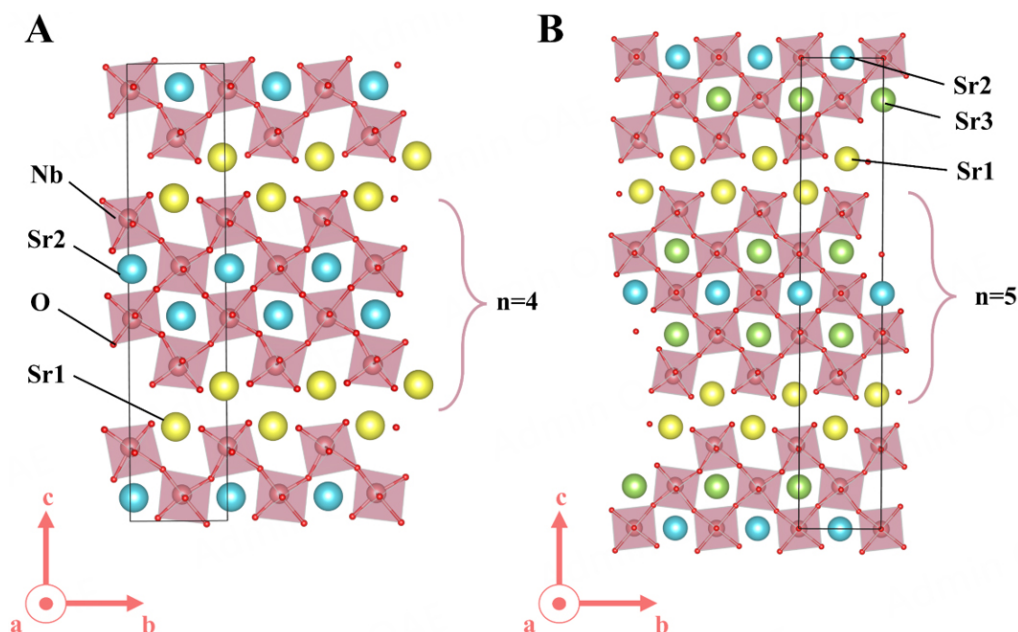
Figure 1. Schematic illustration of crystal structures: (A) 4-layer $Sr_2Nb_2O_7$ and (B) 5-layer $Sr_5Nb_5O_{17}$.

doping may be an effective way to create oxygen vacancies and investigate their impact on conductivity. In contrast to previous reports, where $Sr_5Nb_5O_{17}$ single crystals were typically prepared using the complex floating zone technique while modulating the valence state of Nb through controlled synthesis atmospheres[7], this work introduces equimolar Ga and Mo co-doping to induce oxygen vacancies via a charge compensation mechanism in 4-layered $Sr_2Nb_2O_7$. This approach successfully yields 5-layered $Sr_5Nb_5O_{17}$ phase polycrystalline powders and the effects of co-doping on the material's physical, structural, and electrical properties have been systematically investigated.

MATERIALS AND METHODS

Synthesis

Samples of $Sr_2Nb_{2-2x}Ga_xMo_xO_{7-0.5x}$ ($x \leq 0.2$) were prepared by a conventional solid-phase reaction method with $SrCO_3$ (99.0%), Nb_2O_5 (99.99%), Ga_2O_3 (99.99%), and MoO_3 (99.90%) as starting materials. After being weighed and repeatedly ground in an alcoholic medium for 2 h, followed by air drying, the well-mixed raw materials were pre-calcined at 1,200 °C for 12 h in the air atmosphere with a heating and cooling rate of 5 °C/min. The pre-calcined powder was then milled and pressed into pellets (diameter: 20 mm, thickness: 4-5 mm) and then sintered at 1,450 °C for 12 h. Next, the calcined powder samples were processed with dilute sulfuric acid solution, then filtered, thoroughly washed with water and dried at room temperature under ambient conditions. The resulting products were reground and pressed into pellets (diameter: 10 mm, thickness: 1-2 mm) and sintered at 1,450 °C for 12 h at a heating and cooling rate of 5 °C/min.

Characterization

X-ray diffraction (XRD) was performed on a Panalytical X'pert Pro X-ray diffractometer with a Cu-Kα radiation source. High-quality laboratory XRD data for Rietveld refinement were collected over a 2θ range from 10° to 80° using an interval of 0.02°. The Pawley and Rietveld refinements of the XRD data were carried out by the Topas-Academic software[29]. The Microstructure and energy disperse spectroscopy (EDS) were performed on a Hitachi (Tokyo, Japan) S4800 scanning electron microscope (SEM). The morphology

and internal structure of the prepared samples were further checked by transmission electron microscopy (TEM), selected area electron diffraction (SAED), and high-resolution transmission electron microscopy (HRTEM) using a JEOL JEM-2100F electron microscope operated at a voltage of 200 kV. Elemental mapping of the materials was obtained through an EDAX detector attached to JEOL-2100F. The electrochemical impedance spectroscopy (EIS) was recorded on the Bio-Logic VSP instrument over a 10^6 to 10^{-1} Hz frequency range. Both surfaces of the samples were coated with platinum paste and fired at 850 °C for 30 min to remove any organic components from the electrodes before EIS measurement. For second harmonic generation (SHG) measurements, laser pulses from a Nd:YAG laser system with a wavelength of 1,064 nm were used as the fundamental light and the second harmonic light with a wavelength of 532 nm was detected in a specular reflection geometry. The samples were irradiated with laser pulses of approximately 10 ns duration at a repetition frequency of 40 Hz. The laser was focused to the diffraction limit using an objective lens with a numerical aperture of 0.2 mm. Polarization-electric field (PE) loops were measured using a ferroelectric tester (TF Analyzer 2000, aixACCT, Germany) (150 °C, 10 Hz frequency).

RESULTS AND DISCUSSION
Phases analysis and purification
X-ray diffraction (XRD) experiments were first performed on the as-made samples from solid-state reaction to investigate the phase compositions for $Sr_2Nb_{2-2x}Ga_xMo_xO_{7-0.5x}$ (x = 0.1, 0.2). As shown in Supplementary Figure 1A, it revealed that there are two main phases, i.e., 4-layered $Sr_2Nb_2O_7$ (PDF#70-0114) phase and 5-layered $Sr_5Nb_5O_{17}$ phase (PDF#83-0603) for the sample $Sr_2Nb_{1.8}Ga_{0.1}Mo_{0.1}O_{6.95}$ (SNGM10). While for the $Sr_2Nb_{1.6}Ga_{0.2}Mo_{0.2}O_{6.9}$ (SNGM20) sample, besides the main phase of 5-layered $Sr_5Nb_5O_{17}$, a secondary phase of $SrMoO_4$ (PDF#85-0809) was observed. Moreover, the HAADF-STEM image and energy dispersive X-ray spectroscopy (EDX) elemental maps of SNGM20 clearly show the segregation of the Mo element, as shown in Supplementary Figure 1B. In the Mo segregated area, much lower Nb and Ga concentrations were detected, while both Sr and O elements showed a homogeneous distribution, suggesting that both the main phase and secondary phase contain Sr and O elements, and the Mo element is exclusively distributed in the secondary phase. HRTEM images are shown in Supplementary Figure 1C. It can be seen that the interplanar spacings in the pink squared area of 0.283 and 1.625 nm can be indexed to the (0 -2 0) and (200) crystal planes of $Sr_5Nb_5O_{17}$ (PDF#83-0603), respectively. The green squared area displays a 0.116 nm d-spacing associated with the (219) plane of $SrMoO_4$ (PDF#85-0809), further confirming the Mo-rich area of the SNGM20 sample to be the $SrMoO_4$ phase.

Endeavor to synthesize pure 5-layered $Sr_5Nb_5O_{17}$ phase by adjusting the sintering temperature or the proportion of Mo failed, as shown in Supplementary Figure 2 for the products of the sample SNGMO20 prepared under some other conditions. Thus, to get pure 5-layered $Sr_5Nb_5O_{17}$ phase samples, a chemical purification method was then applied. For this method, the SNGM20 sample was simply fully washed with dilute sulfuric acid (in which the $SrMoO_4$ was soluble while the niobate insoluble) and followed with liquid-solid separation by filtering three times. The subsequent XRD and TEM/EDX measurements confirmed the pure 5-layered $Sr_5Nb_5O_{17}$ phase nature of the yielded dried powders. As shown in Figure 2A and B, all the diffraction peaks in the XRD pattern of the washed sample can be well indexed by the 5-layered $Sr_5Nb_5O_{17}$ phase (PDF#83-0603), and no extra peaks from the secondary phase were identified. In addition, obvious segregation of the Mo element was no longer disclosed by the TEM/EDX characterizations on many different areas of the sample, although there was still very weak signal from the Mo element indicating trace concentration in the sample, as shown in Figure 2C for a selected area. Such trace Mo element may originate from the light surface contamination of the insoluble 5-layered $Sr_5Nb_5O_{17}$ phase powders with the $SrMoO_4$ solution. Such surface contamination is inevitable and the surface trace $SrMoO_4$ is, therefore, hard to remove completely. Nevertheless, this slight surface contamination was thought to have little, if any, impact on the bulk properties of the 5-layered $Sr_5Nb_5O_{17}$ phase sample. Selected area electron diffraction
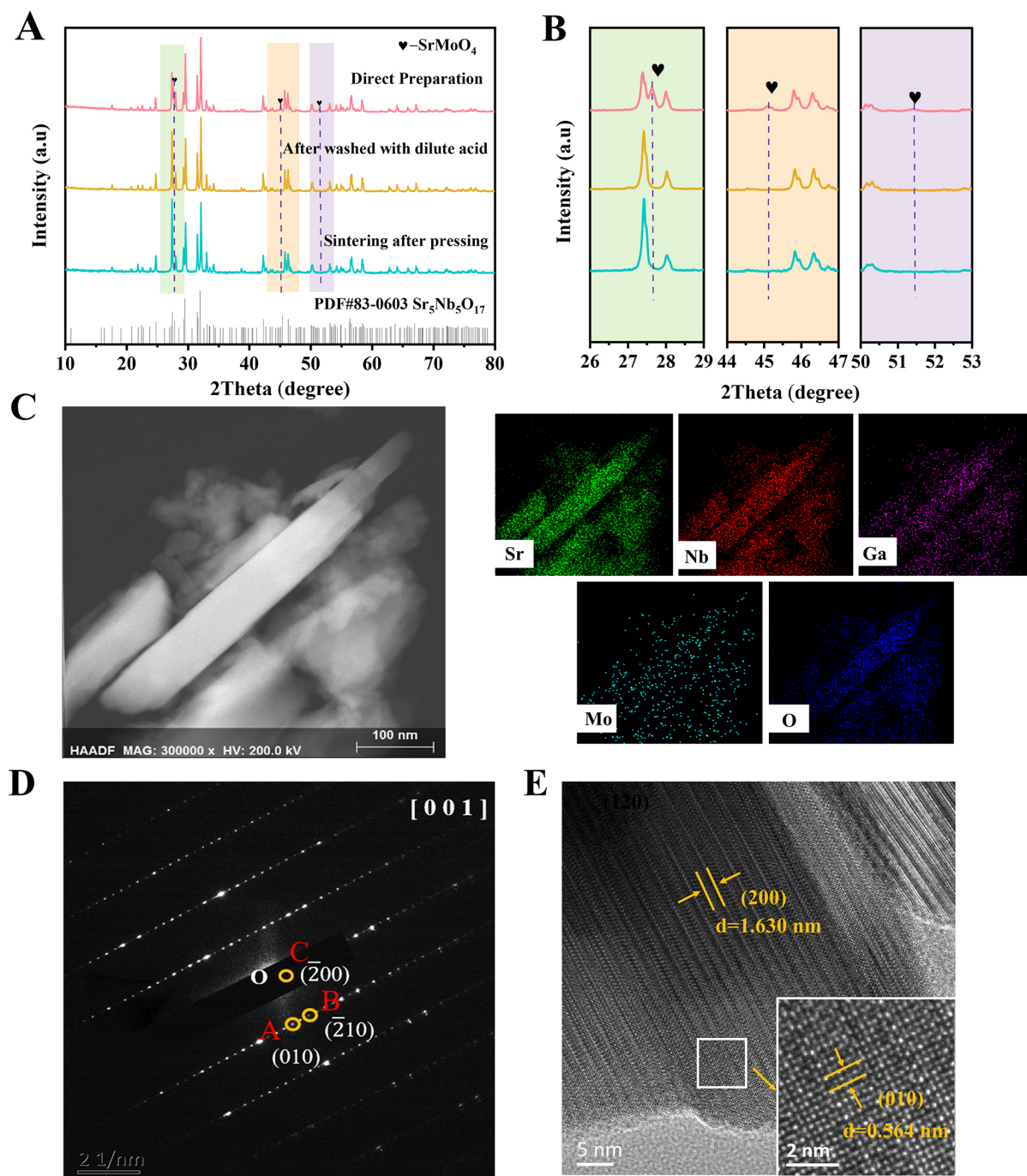
Figure 2. (A) XRD patterns of SNGM20 samples before and after washing; (B) Local enlargement of the XRD spectrum in (A); (C) High-angle annular dark field (HAADF) images and energy dispersive spectroscopy (EDS) mapping of SNGM20 powder after washing; SAED (D) and (E) HRTEM images of the SNGM20 powder after washing.

(SAED) further confirmed the 5-layered structure of the purified sample. As demonstrated in Figure 2D, the electron diffraction pattern from the [001] projection direction can be well indexed to the noncentrosymmetric 5-layer structured $Sr_5Nb_5O_{17}$ phase with space group Pnn2. The measured interplanar spacings in Figure 2E correspond to the (200) and (010) crystallographic planes of $Sr_5Nb_5O_{17}$ (ICSD#79699), respectively. A comparison of HRTEM images of the 5-SNGO and 4-SNO samples

[Supplementary Figure 3] clearly revealed the characteristic lattice spacings: ~1.630 nm of the (200) plane for the 5-layered structure and 1.342 nm of the (020) plane for the 4-layered structure, respectively.

As the Mo element failed in the substitution for Nb and existed in the form of $SrMoO_4$, a more exact composition of the purified 5-layered $Sr_5Nb_5O_{17}$ phase sample may be written as $Sr_{1.8}Nb_{1.6}Ga_{0.2}O_{6.1}$ (viewed as the consequence of subtracting the Mo-containing part of $Sr_{0.2}Mo_{0.2}O_{0.8}$ from the designed initial composition of $Sr_2Nb_{1.6}Ga_{0.2}Mo_{0.2}O_{6.9}$) and normalized as $Sr_5Nb_{4.444}Ga_{0.556}O_{16.944}$ (or $Sr_2Nb_{1.78}Ga_{0.22}O_{6.78}$). This chemical composition was further supported by the Rietveld refinements for the high-resolution XRD data. For the Rietveld refinements, we used the initial orthorhombic 5-layered $Sr_5Nb_5O_{17}$ structure model reported by Schmalle *et al.* with the space group Pnn2 and containing three Sr sites (two 4c sites and one 2b site), three Nb sites (two 4c sites and one 2a site), and nine oxygen sites[8]. The refinement results revealed that the Ga ions were preferred distributed on the Nb1 site (2a) with an occupancy of about 0.549, with the sum of the occupancy of Nb and Ga constrained to be 1.0 on this site. The other Nb sites and Sr sites are all exclusively occupied by Nb and Sr, respectively, with occupancies close to or even larger than 1.0. For the oxygen sites, although their positions were freely refined, the occupancies of these sites were simply set to be one without being refined, due to their weak scattering power to X-ray. The fitting plots are shown in Figure 3 and the final refined structural parameters are summarized in Supplementary Table 1. The refined cation composition of $Sr_5Nb_{0.452(2)}Ga_{0.548(2)}$ further confirmed our above speculation for the actual composition of the purified 5-layer $Sr_5Nb_5O_{17}$ phase sample (denoted as 5-SNGO hereafter). However, when we tried to synthesize the Mo-free and Ga-doped $Sr_2Nb_{2-y}Ga_yO_{7-y}$ samples, although single-phase products can be obtained for the samples $x \le 0.15$, they crystallized in the 4-layer $Sr_2Nb_2O_7$ structure, as shown in Supplementary Figure 4.
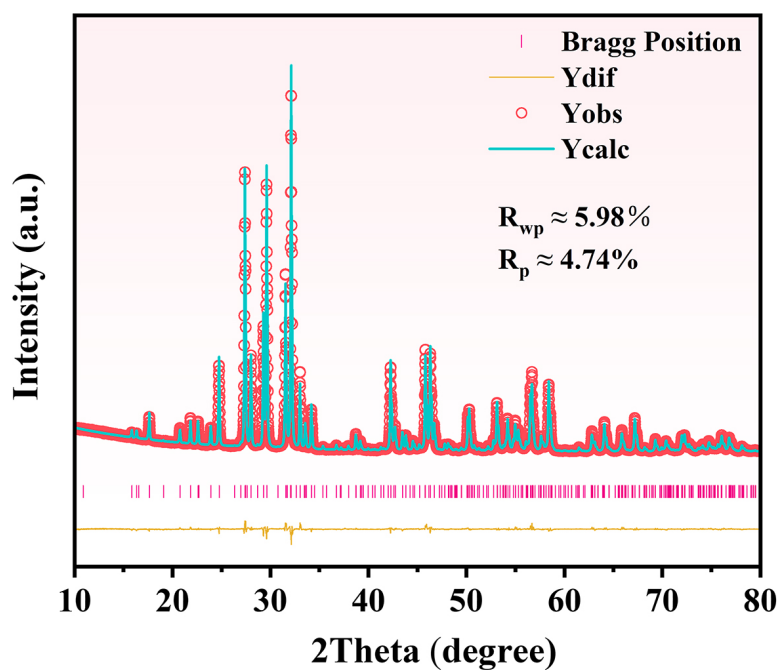
Therefore, it seems that the addition of Mo element is beneficial for the formation of the 5-layer $Sr_5Nb_5O_{17}$ phase. In fact, as had been well documented, the crystallized structure type of the $SrNbO_x$ system is closely related to the oxygen content x, e.g., $SrNbO_{3.5}$ and $SrNbO_{3.4}$ for the 4-layered $Sr_2Nb_2O_7$ and 5-layered $Sr_5Nb_5O_{17}$, respectively. Herein, for the prepared Ga single-doped materials $Sr_2Nb_{2-y}Ga_yO_{7-y}$, the lowest oxygen content for the sample $y = 0.15$ was $SrNbO_{3.425}$, higher than the up-limit ($SrNbO_{3.42}$)[8] for a stable 5-layered structure. Hence, only a 4-layered $Sr_2Nb_2O_7$ phase was identified for these Ga single-doped $Sr_2Nb_{2-y}Ga_yO_{7-y}$ materials. However, for the 5-SNGO ($Sr_5Nb_{4.444}Ga_{0.556}O_{16.944}$) sample, the oxygen content was $SrNbO_{3.39}$, even lower than that ($SrNbO_{3.4}$) for the parent $Sr_5Nb_5O_{17}$ and therefore forming the 5-layered structure. This is interesting and the Mo element, therefore, seems to facilitate the formation of a 5-layer phase by improving the Ga-doping level and accordingly decreasing the oxygen content in the $SrNbO_x$ system, although the exact mechanism of how the Mo element improved the Ga-doping level remained unclear. Additionally, it is worth noting that although the existence of Mo promotes the formation of the 5-layer phase, single Mo doping in $Sr_2Nb_{2-x}Mo_xO_{7+0.5x}$ ($x = 0.1, 0.2$) led to a 4-layer phase (with a minor impurity of $SrNb_8O_{14}$ in both samples, as shown in Supplementary Figure 5) but not a 5-layer structure, which may be attributed to the fact that Mo donor doping at Nb sites is expected to introduce excess oxygen rather than oxygen vacancies into the structure, thereby preventing the formation of an oxygen-deficient 5-layer phase. Nevertheless, the reason for this intriguing Mo doping behavior in the $SrNbO_x$ system remains unknown.

Defect formation energy calculations

To get a fundamental understanding of the solid solution behavior of Ga doped at the Nb site, defect formation energies were calculated using static lattice atomistic simulations based on the General Utility Lattice Program (GULP)[30,31]. The Buckingham potential function was used to model the interaction between ions with the shell model to describe the electronic polarizability for the structural modeling. The potential parameters used for the atomistic simulation are listed in Table 1 and the well-reproducing
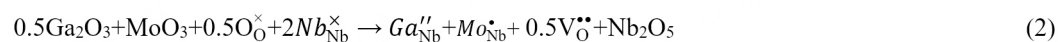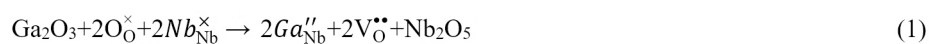
Table 1. Potential parameters used for the atomistic simulation

Interaction	A (eV)	ρ (Å)	C (eV Å⁶)	k (eV Å⁻²)	Y (e)
Sr^{2+} - O^{2}	1,228.9	0.354068	0.0	34	0.74
Nb^{5+} - O^{2-}	1,886.3	0.332637	0.0	1,358.58	11.097
O^{2-} - O^{2-}	334,191.667122	0.216874	701.636798	33.909567	0.04
Ga^{3+} - O^{2-}	1,625.72	0.3019	0.0	-	3.0
Mo^{6+} - O^{2-}	797.47721	0.435484	0.0	147.51	0.11

Figure 3. The Rietveld fitting plots of the SNGM20 powder after washing.

experimentally observed crystal structures (see Table 2) validate the feasibility of these interatomic potential parameters.

Then, the energetics of substitutions was calculated for the single Ga doping, as well as the Ga and Mo co-doping on the Nb site, with the creation of oxygen vacancies as charge compensating defects. This doping process of Ga for Nb and Ga/Mo co-doping for Nb can be represented by the following defect reactions (1) and (2), respectively:

$$Ga_2O_3 + 2O_O^\times + 2Nb_{Nb}^\times \rightarrow 2Ga_{Nb}'' + 2V_O^{\bullet\bullet} + Nb_2O_5 \tag{1}$$

$$0.5Ga_2O_3 + MoO_3 + 0.5O_O^\times + 2Nb_{Nb}^\times \rightarrow Ga_{Nb}'' + Mo_{Nb}^\bullet + 0.5V_O^{\bullet\bullet} + Nb_2O_5 \tag{2}$$

The energies of this solid solution reaction can be evaluated by combining the appropriate point defect energy and lattice energy terms. The point defect energies and lattice energies are summarized in Table 3. We can see that the lowest oxygen vacancy formation energy was calculated to occur at the O5 position, suggesting the most likely position for oxygen vacancy. The solid solution energies of Ga substitution for Nb, as well as Ga and Mo co-doping for Nb, in the 5-layered $Sr_5Nb_5O_{17}$ structure, are summarized in

Table 2. Calculated and experimental structural parameters for $Sr_5Nb_5O_{17}$

Parameters	Calculated	Experimental	Difference (Calc. - Exp.)
a (Å)	32.4560	32.5510	0.0950
b (Å)	5.6740	5.5852	-0.0887
c (Å)	3.9950	3.9313	-0.0636
Mean Nb1 - O (Å)	2.0061	1.9724	-0.0336
Mean Nb2 - O (Å)	2.0143	2.0048	-0.0095
Mean Nb3 - O (Å)	2.0065	1.9981	-0.0084
Mean Sr1 - O (Å)	2.4972	2.4508	-0.0463
Mean Sr2 - O (Å)	2.7349	2.6211	-0.1138
Mean Sr3 - O (Å)	2.7254	2.6339	-0.0915

Table 3. Energy of various lattices and defects

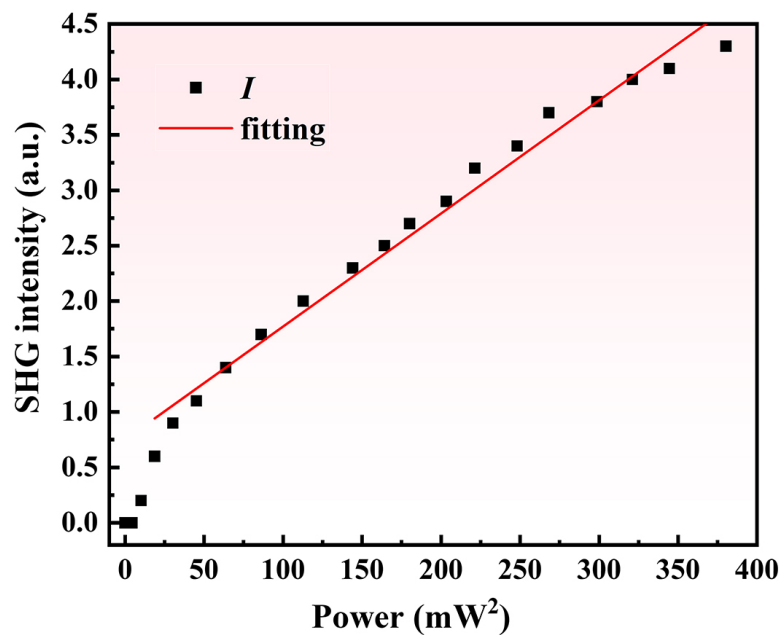| Defect	Energy (eV)	Defect	Energy (eV)
$V_{O1}^{\bullet\bullet}$	32.70	Nb_2O_5 (Z = 14)	-4,742.54
$V_{O2}^{\bullet\bullet}$	32.84	Ga_2O_3 (Z = 6)	-925.78
$V_{O3}^{\bullet\bullet}$	34.97	MoO_3 (Z = 8)	-1,675.04
$V_{O4}^{\bullet\bullet}$	22.27	Ga_{Nb1}''	62.06
$V_{O5}^{\bullet\bullet}$	22.23	Ga_{Nb2}''	69.27
$V_{O6}^{\bullet\bullet}$	28.59	Ga_{Nb3}''	64.19
$V_{O7}^{\bullet\bullet}$	23.10	$Mo_{Nb1}^{\bullet}$	-36.65
$V_{O8}^{\bullet\bullet}$	27.36	$Mo_{Nb2}^{\bullet}$	-41.62
$V_{O9}^{\bullet\bullet}$	32.55	$Mo_{Nb3}^{\bullet}$	-38.36

Table 4, with the oxygen vacancy supposed to be created at the O5 position due to its lowest point defect formation energy as shown in Table 3. The results show that the solid solution energies of Ga doping at the Nb1, Nb2, and Nb3 sites are -15.8931, -1.4693, and -11.6292 eV, respectively, indicating the Ga atoms are preferred to occupy the Nb1 position, which has the highest symmetry among the three Nb sites, and this is in good agreement with the results from Rietveld refinements for the XRD data. In contrast, for Ga and Mo co-doping for Nb1, Nb2 and Nb3 sites, the final calculated solid solution energies are 17.6358, 19.8798, and 18.0536 eV, respectively, which is apparently higher than that of the single Ga doping, which well explains experimentally observed behaviors that the Ga and Mo co-doping failed to obtain single phase and only Ga succeeded in substitution for Nb atoms in the 5-layered $Sr_5Nb_5O_{17}$ phase.

Nonlinear optical properties

An optical second harmonic generation (SHG) measurement method was then utilized to investigate the symmetry of the purified sample 5-SNGO. The SHG has a high sensitivity to symmetry breaking and can be used to study the symmetry, ferroelectricity, and ferromagnetism of materials and to determine the phase transition temperature[32,33]. Non-centrosymmetry (NCS) is the prerequisite for an SHG process because the SHG coefficient is zero ($\chi^2 = 0$) in all centrosymmetric materials. Therefore, ferroelectric states that do not have inversion symmetry usually provide strong second-harmonic signals, which display second-order nonlinear optical behavior. The SHG plot of the 5-SNGO sample is shown in Figure 4. It can be seen that as the incident light power increases, it needs to pass through a threshold power, which corresponds to the power point where the signal begins to significantly enhance. When the incident optical power squared is greater than 50 mW^2, the intensity of the SHG is proportional to the incident light power squared and exhibits second-order nonlinear optical behavior, consistent with the noncentrosymmetric structure with the space group Pnn2.

Table 4. The extrinsic and intrinsic defect formation energies

Defect type	Equation	Energy (eV)
Acceptor-doping	$Ga_2O_3 + 2O_O^\times + 2Nb_{Nb}^\times \rightarrow 2Ga_{Nb1}'' + 2V_{O5}^{\bullet\bullet} + Nb_2O_5$	-15.89
Acceptor-doping	$Ga_2O_3 + 2O_O^\times + 2Nb_{Nb}^\times \rightarrow 2Ga_{Nb2}'' + 2V_{O5}^{\bullet\bullet} + Nb_2O_5$	-1.47
Acceptor-doping	$Ga_2O_3 + 2O_O^\times + 2Nb_{Nb}^\times \rightarrow 2Ga_{Nb3}'' + 2V_{O5}^{\bullet\bullet} + Nb_2O_5$	-11.63
Acceptor-doping	$0.5Ga_2O_3 + MoO_3 + 0.5O_O^\times + 2Nb_{Nb}^\times \rightarrow Ga_{Nb1}'' + Mo_{Nb1}^\bullet + 0.5V_{O5}^{\bullet\bullet} + Nb_2O_5$	17.64
Acceptor-doping	$0.5Ga_2O_3 + MoO_3 + 0.5O_O^\times + 2Nb_{Nb}^\times \rightarrow Ga_{Nb2}'' + Mo_{Nb2}^\bullet + 0.5V_{O5}^{\bullet\bullet} + Nb_2O_5$	19.88
Acceptor-doping	$0.5Ga_2O_3 + MoO_3 + 0.5O_O^\times + 2Nb_{Nb}^\times \rightarrow Ga_{Nb3}'' + Mo_{Nb3}^\bullet + 0.5V_{O5}^{\bullet\bullet} + Nb_2O_5$	18.05

Figure 4. SHG intensity as a function of the incident light power squared in the 5-SNGO sample.

Ferroelectric measurements

Figure 5A and B shows the ferroelectric hysteresis loops of $Sr_2Nb_2O_7$ (4-SNO) and 5-SNGO measured at 150 °C, 10 Hz frequency, under different electric fields. Figure 5C and D shows the polarization-electric field (*P-E*) hysteresis loops and charging current density-electric field (*I-E*) curves for 4-SNO and 5-SNGO ceramics at an electric field of 150 kV/cm. For the 4-SNO sample, saturated *P-E* hysteresis loops and obvious peaks in the *I-E* curves are observed, confirming its ferroelectricity. When the coercive field (E_c) is applied, the I-E peak appears, indicating ferroelectric domain switching. The 4-SNO sample has a spontaneous polarization strength (P_s) of 4.09 μC/cm², a remanent polarization (P_r) of 1.17 μC/cm², and a corresponding coercive field (E_c) of 33.52 kV/cm. For the 5-SNGO sample, no *I-E* peak is detected, indicating that it exhibits paraelectric behavior.

Dielectric studies

Figure 6 displays the frequency dependence of the dielectric constant (ε') and dielectric loss ($\tan\delta$) for samples 4-SNO and 5-SNGO at room temperature. We can see that as the frequency increases from 10^2 to $\sim10^5$ Hz, the dielectric constant decreases sharply (from ~280 to ~90) for the 4-SNO sample, indicating dispersive behavior. Then, the ε' reaches a constant value at higher frequencies. However, for the 5-SNGO sample, only a slight decrease in ε' (from ~100 to ~60) was observed within a much more narrow frequency range of 10^2 to $\sim10^3$ Hz, and then it kept stable. Usually, for a given sample, the relatively higher values
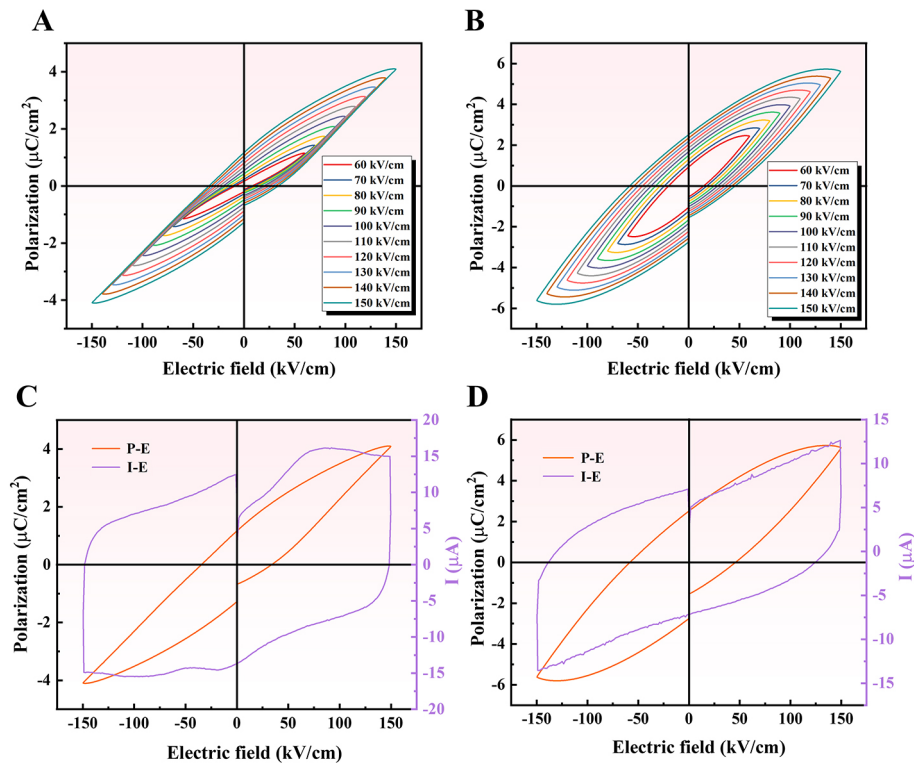
Figure 5. Polarization-electric field hysteresis loops (*P-E*) of (A) 4-SNO and (B) 5-SNGO measured at 150 °C, 10 Hz frequency, under different electric fields. Polarization-electric field (*P-E*) hysteresis loops and charging current density-electric field (*I-E*) curves for (C) 4-SNO and (D) 5-SGNO samples at 150 °C, 10 Hz frequency.

observed at low frequencies may be attributed to the space charge polarization, such as the Maxwell-Wagner effect. The dielectric constant decreases with increasing frequency can be explained by the fact that in a high-frequency electric field, the polarization response could not keep up with the change in the electric field direction, resulting in a decrease in the degree of polarization. For dielectric loss, similar behaviors were also observed that at the low-frequency range, the tanδ of the 5-SNGO sample showed a sharper decrease from 0.60 to 0.006 within the frequency range of 10^2 to $\sim 10^5$ Hz, while the 4-SNO sample decreased from 0.20 to 0.001 within almost the same frequency range. At higher frequencies, the tanδ kept stable for both samples. The higher dielectric losses at low frequencies are related to the grain boundary defects[34]. Thus, generally speaking, the ε′ and tanδ of the 4-SNO sample are higher than those of the 5-SNGO sample, especially at the low-frequency range, but the 5-SNGO sample displayed better frequency stabilities compared to the 4-SNO sample. Polarization studies show that 5-SNGO has a slightly lower dielectric constant and dielectric loss than 4-SNGO, possibly related to the concentration of oxygen vacancies created by the substitution of Ga for Nb ions. The formation of oxygen vacancies reduces dielectric loss and improves frequency stability. Therefore, the more flattened dielectric constant and lower dielectric loss of the 5-SNGO sample offer better possibilities for applications compared to the classical 4-SNO sample.

Complex impedance

To investigate the contribution of defective dipole/oxygen vacancies to the electrical properties of 5-SNGO, the complex impedance spectroscopy technique was also applied. Figure 7A shows the complex impedance spectra of the 5-SNGO ceramics, measured over the temperature range of 750 to 900 °C. It can be observed from the figure that only one semicircular arc is observed in the impedance spectrum, which indicates that the ceramic is mainly affected by the grain response and that the resistance of the ceramic decreases with
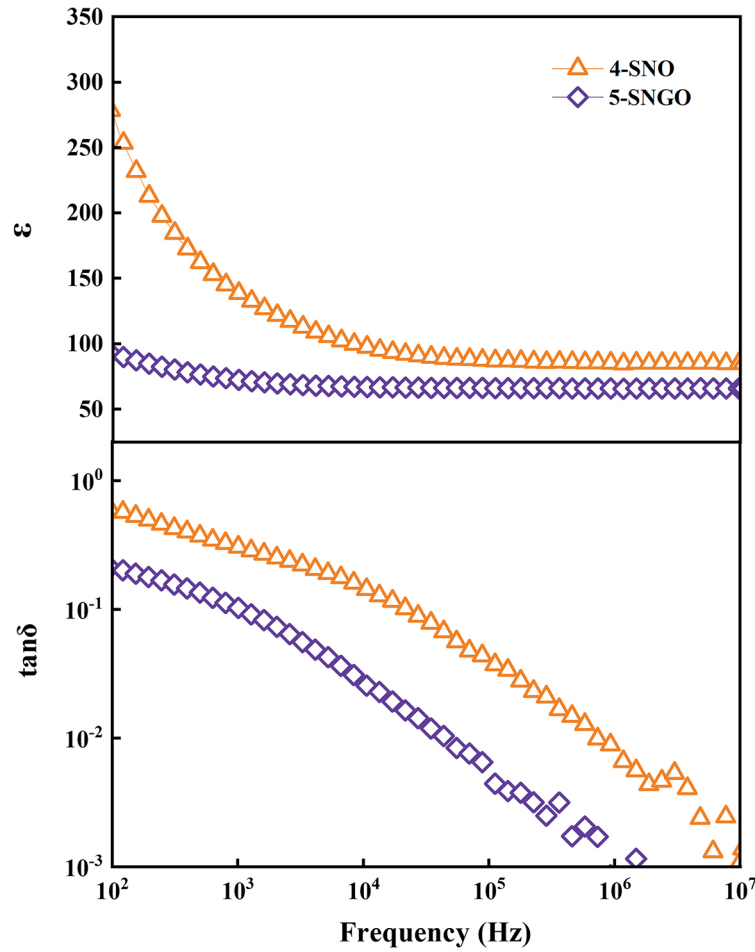
Figure 6. Frequency dependence of the real (ε') parts of dielectric permittivity and dielectric loss (tan) of 4-SNO and 5-SNGO ceramics at room temperature.

increasing temperature, corresponding to the negative temperature coefficient effect of the ceramic resistor[35], and that the increase in the AC conductivity suggests the thermally activated process of the defective carriers. The DC resistivities of both the 4-SNO and 5-SNGO samples in the range of 600-900 °C are shown in Figure 7B, from which it can be clearly observed that the 5-SNGO ceramic has a resistivity approximately two orders of magnitude higher than that of the 4-SNO, e.g., 1.95×10^5 *vs.* 1.73×10^3 Ω·cm at 900 °C, for 5-SNGO and 4-SNO, respectively. Thus, 5-SNGO material has an apparently enhanced insulating property compared to that of the 4-SNO material. A further study of the dielectric relaxation process and activation energy changes in the 5-SNGO ceramic can be achieved through the analysis of the normalized imaginary impedance Z''/Z''_{max} [Figure 7C]. The 5-SNGO sample exhibits only one peak in the investigated frequency and temperature range and shows excellent symmetry at each temperature. Meanwhile, at high temperatures, the carrier hopping movement is accelerated and the peaks are shifted toward the high-frequency region, which can be attributed to the thermally activated jumps of the carriers (oxygen vacancies). Arrhenius fitting of the peaks was performed using the following equation[36]:

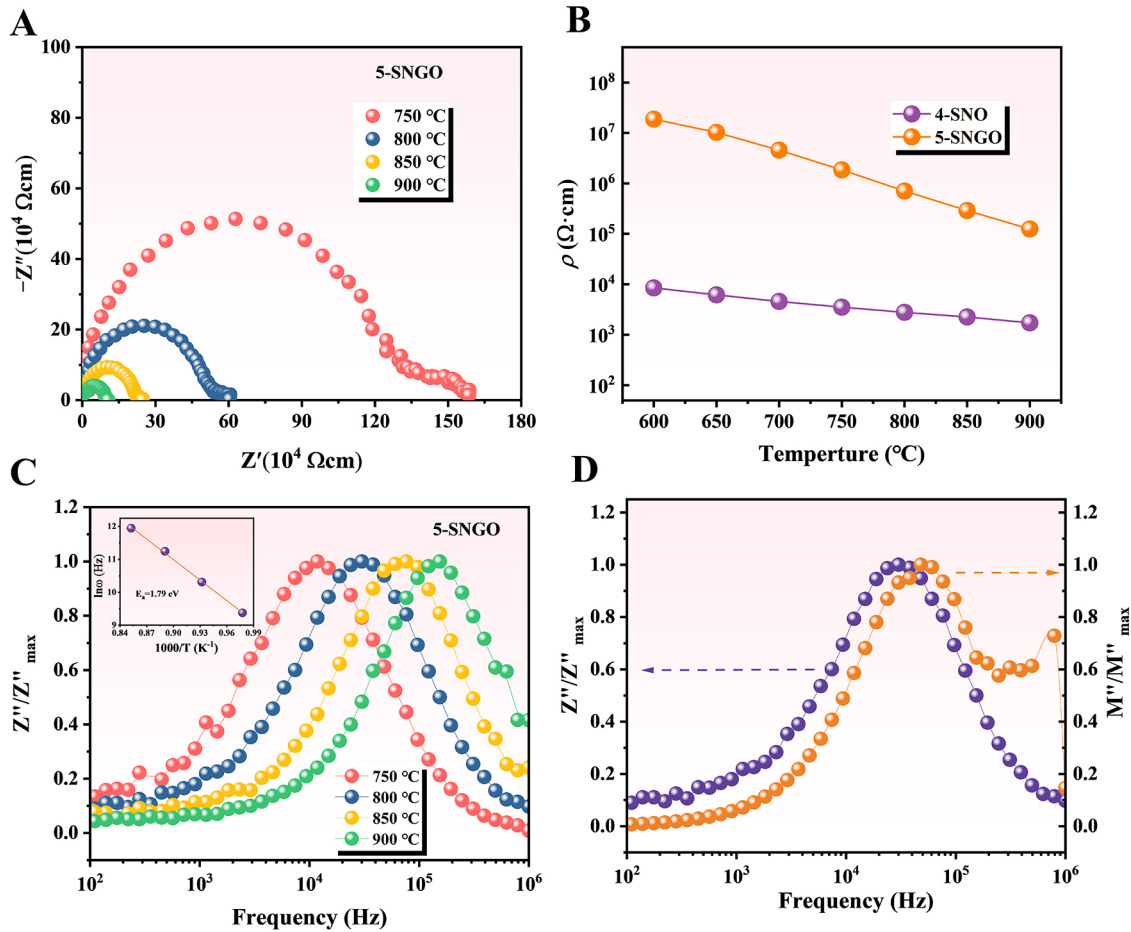$$\omega_{max} = \omega_0 \exp\left(\frac{E_a}{k_B T}\right) \tag{3}$$

Figure 7. (A) Complex plane impedance plots of 5-SNGO recorded at temperatures 750-900 °C; (B) direct current (DC) resistivity of 4-SNO and 5-SNGO ceramics; (C) frequency dependence of normalized impedance Z''/Z''_{max} of 5-SNGO; (D) the relationship of Z''/Z''_{max} and M''/M''_{max} at 800 °C of 5-SNGO.

where ω_0, E_a, k_B, and T denote the pre-exponential factor, the relaxation activation energy of imaginary impedance Z'', the Boltzmann constant (8.617×10^{-5} eV/K), and the Kelvin temperature, respectively. The relaxation activation energy E_a can be obtained from the data points in the plot of $\ln(\omega)$ versus $1,000/T$ by linear fitting, as shown in the inset of Figure 7C. The E_a of SNGMO ceramics is 1.79 eV at 750-900 °C. Ang *et al.* concluded that the high-temperature relaxation in many perovskite-like structures is caused by the long-range migration of oxygen vacancies[37]. In contrast, for high-temperature insulating materials, the higher relaxation activation energy contributes to the insulation stability at elevated temperatures, prevents excessive charge-carrier mobility, and improves the potential for applying this ceramic at extreme temperatures. Figure 7D shows the Z''/Z''_{max} *vs.* f and M''/M''_{max} *vs.* f curves for 5-SNGO ceramic at 800 °C. It is noticed that the Z''/Z''_{max} and M''/M''_{max} peaks do not completely overlap but are very close to each other, suggesting contributions from both long-range and localized relaxation effects[38]. Comparison of the impedance and modulus data allows us to rationalize the subject response on the basis of local (dielectric relaxation) and non-local (ionic conductivity) relaxation processes.

CONCLUSIONS

In this work, a novel 5-layered $Sr_5Nb_5O_{17}$ phase material with the chemical composition of $Sr_5Nb_{4.444}Ga_{0.556}O_{16.944}$ (5-SNGO) was synthesized by solid-state reaction method followed by a chemical

purification route, and its physical, structural, and electrical properties were investigated. The results revealed that the addition of the Mo element helped improve the Ga-doping level in $Sr_2Nb_2O_7$ and decreased the oxygen content to $SrNbO_{3.39}$ and, therefore, formed the 5-layered phase, although the Mo element did not finally enter the structure of this 5-layer material and existed in the form of $SrMoO_4$ as a secondary phase. The crystal structure of 5-SNGO was confirmed to be noncentrosymmetrical with the space group Pnn2, exhibiting second-order nonlinear optical behavior. The dielectric permittivity of 5-SNGO ceramic is constant at 60, independent of frequency above 1 kHz. The impedance spectra of the 5-SNGO ceramic exhibit Debye-like dielectric relaxation behavior and a higher resistivity of 1.95×10^5 Ω·cm at 900 °C compared to that of 4-SNO.

DECLARATIONS

Authors' contributions
Sample fabrication and characterization: Duan, X.
Performed the experiments and data analysis: Duan, X.; Xu, J.; Yang, X.; He, X.; Wang, C.
Preparation of the manuscript and discussion: Duan, X.; Xu, J.; Liu, L.

Availability of data and materials
All data and materials included in this study are available from the corresponding authors upon reasonable request.

Financial support and sponsorship

Conflicts of interest
He, X., from China Nonferrous Metals (Guilin) Geology And Mining Co., Ltd, assisted with second harmonic generation (SHG) measurements using her company's instruments, while the other authors have declared that they have no conflicts of interest.

Ethical approval and consent to participate
Not applicable.

Consent for publication
Not applicable.

Copyright

REFERENCES

1. Ladasiu, C.; Kulischow, N.; Marschall, R. Tuning the photocatalytic activity of layered perovskite niobates by controlled ion exchange and hydration. *Catal. Sci. Technol.* **2022**, *12*, 1450-7. DOI
2. Kulischow, N.; Ade, M.; Weiss, M.; Marschall, R. Nitrogen-doped, proton-exchanged Dion-Jacobson layered niobate perovskites for photocatalytic hydrogen generation in solar light. *Photochem. Photobiol. Sci.* **2022**, *21*, 1991-2000. DOI PubMed
3. Xia, R.; Chen, J.; Liang, R.; Zhou, Z. The positive effect of A-site nonstoichiometry on the electrical properties of $Sr_2Nb_2O_7$ ceramics for high temperature piezoelectric sensor application. *Ceram. Int.* **2022**, *48*, 22459-67. DOI
4. Pan, C.; Zhang, J. C.; Zhang, M.; et al. Trap-controlled mechanoluminescence in Pr^{3+}-activated $M_2Nb_2O_7$ (M = Sr, Ca) isomorphic perovskites. *Opt. Mater. Express.* **2018**, *8*, 1425-34. DOI
5. Kodera, M.; Moriya, Y.; Katayama, M.; Hisatomi, T.; Minegishi, T.; Domen, K. Investigation on nitridation processes of $Sr_2Nb_2O_7$ and

SrNbO$_3$ to SrNbO$_2$N for photoelectrochemical water splitting. *Sci. Rep.* **2018**, *8*, 15849. DOI PubMed PMC

6.   Guo, Y.; Guo, W.; Lei, L.; Xu, J. Oxide ion conduction and transporting mechanism in the layered perovskite-related material Sr$_2$Nb$_2$O$_7$. *Scripta. Mater.* **2022**, *221*, 114962. DOI

7.   Sakai, A.; Kanno, T.; Takahashi, K.; Yamada, Y.; Adachi, H. Large anisotropic thermoelectricity in perovskite related layered structure: Sr$_n$Nb$_n$O$_{3n+2}$ (*n* = 4, 5). *J. Appl. Phys.* **2010**, *108*, 103706. DOI

8.   Schmalle, H. W.; Williams, T.; Reller, A.; Lichtenberg, F.; Widmer, D.; Bednorz, J. G. A novel semiconducting perovskite-related phase: Sr$_5$Nb$_5$O$_{17}$. *Acta. Cryst. C. Cryst. Struct. Commun.* **1995**, *51*, 1243-6. DOI

9.   Kuntscher, C. A.; Schuppler, S.; Haas, P.; et al. Extremely small energy gap in the quasi-one-dimensional conducting chain compound SrNbO$_{3.41}$. *Phys. Rev. Lett.* **2002**, *89*, 236403. DOI

10. Abrahams, S. C.; Schmalle, H. W.; Williams, T.; et al. Centrosymmetric or Noncentrosymmetric? Case study, generalization and structural redetermination of Sr$_5$Nb$_5$O$_{17}$. *Acta. Cryst. B. Struct. Sci.* **1998**, *54*, 399-416. DOI

11. Zhou, Z.; Chen, T.; Liu, X.; Liang, R. Phase transitions and ferroelectricity of perovskite layered Sr$_2$Nb$_2$O$_7$ ceramics. *J. Phys. Chem. Solids.* **2022**, *169*, 110888. DOI

12. Song, Y. M.; Dai, J. Q.; Zhang, H. Influence of oxygen vacancy on electric structure and optical properties of pure and N-doped Sr$_2$M$_2$O$_7$ (M = Nb, Ta). *Comput. Mater. Sci.* **2017**, *127*, 180-6. DOI

13. Chen, T.; Liang, R.; Jiang, K.; Hu, Z.; Zhou, Z.; Dong, X. Low-temperature sintering and electrical properties of Sr$_2$Nb$_2$O$_7$ piezoceramics by CuO addition. *J. Am. Ceram. Soc.* **2017**, *100*, 2397-401. DOI

14. Cai, X.; Teng, Y.; Wu, L.; Zhang, K. Hot-press sintering Sr$_2$Nb$_2$O$_7$ ceramics and their electrical properties. *J. Mater. Sci. Mater. Electron.* **2017**, *28*, 4239-44. DOI

15. Liou, Y. C.; Tsai, W. C.; Yu, J. Y. Effects of La addition on properties of Sr$_2$Nb$_2$O$_7$ thermoelectric ceramics. *J. Electron. Mater.* **2015**, *44*, 4857-63. DOI

16. Ojeda-Galván, H. J.; Rodríguez-Aranda, M. D. C.; Rodríguez, Á. G.; et al. Structural and Raman study of the thermoelectric solid solution Sr$_{1.9}$La$_{0.1}$Nb$_2$O$_7$. *J. Raman. Spectrosc.* **2021**, *52*, 737-49. DOI

17. Chen, G.; Gong, C. W.; Fu, C. L.; et al. Microstructure and dielectric properties of (Ba, Ta) Co-doped Sr$_2$Nb$_2$O$_7$ ceramics. *Mater. Sci. Forum.* **2015**, *815*, 125-8. DOI

18. Xiang, L.; Chen, G.; Fu, C.; Cai, W.; Wang, W.; Liu, K. Effect of Ta doping on the microstructure, dielectric and ferroelectric properties of Sr$_2$Nb$_2$O$_7$ ceramics. *Ferroelectrics* **2014**, *467*, 165-72. DOI

19. Yuan, Y.; Han, X.; Dong, H.; Zhou, X. First-principles calculation of chalcogen-doped Sr$_2$M$_2$O$_7$ (M=Nb and Ta) for visible light photocatalysis. *J. Solid. State. Chem.* **2022**, *308*, 122905. DOI

20. Geng, J.; Chen, Y.; Gu, G.; Tian, L. Tunable white-light-emitting Sr$_{2-x}$Ca$_x$Nb$_2$O$_7$:Pr^{3+} phosphor by adjusting the concentration of Ca^{2+} ion. *Opt. Mater.* **2014**, *36*, 1093-6. DOI

21. Wang, C. M.; Wang, J. F.; Zhang, S.; Shrout, T. R. Piezoelectric and electromechanical properties of ultrahigh temperature CaBi$_2$Nb$_2$O$_9$ ceramics. *Phys. Rapid. Res. Lett.* **2009**, *3*, 49-51. DOI

22. Peng, Z.; Chen, L.; Xiang, Y.; Cao, F. Microstructure and electrical properties of lanthanides-doped CaBi$_2$Nb$_2$O$_9$ ceramics. *Mater. Res. Bull.* **2022**, *148*, 111670. DOI

23. Gavin, A. L.; Watson, G. W. Defects in orthorhombic LaMnO$_3$ - ionic *versus* electronic compensation. *Phys. Chem. Chem. Phys.* **2018**, *20*, 19257-67. DOI PubMed

24. Lichtenberg, F.; Herrnberger, A.; Wiedenmann, K.; Mannhart, J. Synthesis of perovskite-related layered A$_n$B$_n$O$_{3n+2}$ = ABO$_X$ type niobates and titanates and study of their structural, electric and magnetic properties. *Prog. Solid. State. Chem.* **2001**, *29*, 1-70. DOI

25. Chen, C.; Yin, D.; Inoue, K.; et al. Atomic-scale origin of the quasi-one-dimensional metallic conductivity in strontium niobates with perovskite-related layered structures. *ACS. Nano.* **2017**, *11*, 12519-25. DOI

26. Chen, C.; Wang, Z.; Lichtenberg, F.; Ikuhara, Y.; Bednorz, J. G. Patterning oxide nanopillars at the atomic scale by phase transformation. *Nano. Lett.* **2015**, *15*, 6469-74. DOI

27. Chen, C.; Lv, S.; Wang, Z.; et al. Atomic and electronic structure of the SrNbO$_3$/SrNbO$_{3.4}$ interface. *Appl. Phys. Lett.* **2014**, *105*, 221602. DOI

28. Fu, C.; Liu, H.; Chen, G.; Cai, W.; Deng, X. Microstructure and electric properties of strontium lanthanum niobate ceramics. *Ferroelectrics* **2012**, *432*, 8-13. DOI

29. Coelho, A. A.; Evans, J.; Evans, I.; Kern, A.; Parsons, S. The TOPAS symbolic computation system. *Powder. Diffr.* **2011**, *26*, S22-5. DOI

30. Gale, J. D.; Rohl, A. L. The general utility lattice program (GULP). *Mol. Simul.* **2003**, *29*, 291-341. DOI

31. Julian, D. G. GULP: a computer program for the symmetry-adapted simulation of solids. *J. Chem. Soc. Faraday. Trans.* **1997**, *93*, 629-37. DOI

32. Ok, K. M.; Chi, E. O.; Halasyamani, P. S. Bulk characterization methods for non-centrosymmetric materials: second-harmonic generation, piezoelectricity, pyroelectricity, and ferroelectricity. *Chem. Soc. Rev.* **2006**, *35*, 710-7. DOI PubMed

33. Fichera, B. T.; Kogar, A.; Ye, L.; et al. Second harmonic generation as a probe of broken mirror symmetry. *arXiv* **2019**, *1909.12850*,. DOI

34. Alange, R. C.; Khirade, P. P.; Birajdar, S. D.; Humbe, A. V.; Jadhav, K. M. Structural, magnetic and dielectrical properties of Al-Cr Co-substituted M-type barium hexaferrite nanoparticles. *J. Mol. Struct.* **2016**, *1106*, 460-7. DOI

35. Xiong, X.; Tian, R.; Lin, X.; Chu, D.; Li, S. Thermoelectric properties of sol-gel derived lanthanum titanate ceramics. *RSC. Adv.* **2015**,

5, 14735-9. DOI

36.   Zheng, X.; Wang, S.; Wang, J.; Hua, W.; Zhang, J.; Liu, L. Long-range and short-range transport dynamics of Li ions in $LiMn_2O_4$. *J. Phys. Chem. C.* **2020**, *124*, 25254-61. DOI

37.   Ang, C.; Yu, Z.; Cross, L. E. Oxygen-vacancy-related low-frequency dielectric relaxation and electrical conduction in $Bi:SrTiO_3$. *Phys. Rev. B.* **2000**, *62*, 228. DOI

38.   Gerhardt, R. Impedance and dielectric spectroscopy revisited: distinguishing localized relaxation from long-range conductivity. *J. Phys. Chem. Solids.* **1994**, *55*, 1491-506. DOI